High-Order Diffractive Elastic-Wave Manipulations Based on Piezoelectric Metasurfaces

Ruitao Li[1], Bochen Ren[1] and Bing Li[1,2,*]

[1]*School of Aeronautics, Northwestern Polytechnical University, Xi'an, Shaanxi, 710072, China*

[2]*National Key Laboratory of Strength and Structural Integrity, Xi'an, China*

Abstact: Elastic metasurfaces offer powerful capabilities for manipulating wave propagation, with applications ranging from vibration attenuation and noise isolation to structural health monitoring. However, the multimodal nature and strong dispersion of elastic-waves impede the realization of stable, broadband control. While piezoelectric materials provide a pathway toward active tunability, the manipulation of higher-order diffracted guided waves remains a significant challenge, restricting practical engineering utility. Here, we propose a tunable piezoelectric elastic metasurface that overcomes these limitations. By adjusting piezoelectric parameters via simple external circuits—without modifying the structural substrate—we demonstrate versatile control over elastic-waves and their higher-order diffraction modes, including adaptive anomalous refraction, tunable subwavelength focusing, source illusion etc. This approach enables diverse exotic wave phenomena, bridging the gap between theoretical research and the practical application of intelligent wave manipulation.

Keyword: Elastic-waves, high-order diffraction, piezoelectric metasurfaces, phase modulation, asymmetric transmission.

1. INTRODUCTION

Plate-shell structures are among the most common lightweight structures in engineering practice. The manipulation of elastic-wave propagation in plates has garnered widespread research interest, particularly in fields such as structural health monitoring, vibration control, and noise isolation [1-4]. As a ultrathin, two-dimensional artificial surface/interface, elastic metasurfaces have emerged as a powerful solution for wavefront engineering [5]. By introducing abrupt phase discontinuities, they enable exotic wave control phenomena, including focusing, anomalous refraction, and asymmetric transmission, without altering the structural geometry or adding significant mass [6-8].

Although elastic metasurfaces provide a versatile platform for controlling elastic-wave propagation, most of their designs achieve specific functions only at particular operating frequencies. Limitations in frequency adaptability and functionality remain significant challenges in current research. To overcome these limitations and achieve frequency-tunable or function-reconfigurable metasurfaces, researchers have introduced various active control mechanisms into metasurface design. By altering the external physical conditions of the plate-shell structure, elastic metasurfaces can achieve better frequency adaptability [9-12]. However, these approaches often suffer from bulky instrumentation, slow response times, and discontinuous tuning ranges. Consequently, piezoelectric metasurfaces based on the electromechanical coupling effect offer a compelling alternative due to their simple structure and continuous tunability. By shunting piezoelectric patches with external circuits—such as inductors or negative capacitance elements—the effective material properties can be continuously modulated, enabling precise control over local resonance bandgaps and wave propagation characteristics via simple electrical adjustments [13, 14].

According to the generalized Snell's law, a non-zero diffracted wave can be obtained only when the incident angle is smaller than the critical angle. However, studies have found that when the incident angle is greater than or equal to the critical angle, the transmitted wave does not simply vanish. Instead, a series of diffracted waves that do not conform to the generalized Snell's law can be observed, a phenomenon referred to as higher-order diffraction [15]. The higher-order diffraction effect and the parasitic noise introduced by higher-order diffracted waves pose significant challenges to precise and efficient wave manipulation. These issues are particularly pronounced in elastodynamics due to the existence of additional wave modes and the inherent mode conversion of elastic-waves. While existing research often neglects the adverse effects of higher-order diffraction or relies on suppression strategies to mitigate its impact, disregarding the active control of higher-order diffracted waves can compromise the accuracy and efficiency of elastic-waveguiding. Recent

studies suggest that harnessing higher-order diffraction can unlock new functionalities, such as efficient asymmetric transmission [16], efficient microwave absorption [5], omnidirectional isolation and ultrathin waveguides [17].

Here, we propose a tunable piezoelectric elastic metasurface that bridges these gaps. We design a unit cell with electrically tunable phase and frequency responses, serving as the building block for a reconfigurable metasurface. Using multiphysics simulations, we demonstrate that adjusting the external circuit parameters enables dynamic control over anomalous refraction and subwavelength focusing. Furthermore, we construct a ring-shaped configuration to realize an acoustic source illusion. Specifically, by incorporating higher-order diffraction theory, we achieve switchable asymmetric transmission, demonstrating that piezoelectric metasurfaces can effectively manipulate not only fundamental but also higher-order diffracted modes. This work establishes a versatile platform for intelligent elastic-wave control, expanding the practical utility of active metasurfaces in complex engineering environments.

2. UNIT CELL MODEL

2.1. Generalized Snell's Law

When waves undergo reflection or transmission at the interface between two media, if it is assumed that the various modes are decoupled, then for high-frequency and short waves, they typically obey Snell's law. However, if the interface itself introduces a phase change to the waves, the original Snell's law no longer applies [18]. When a metasurface is introduced at the interface between two media, assuming it can modify the phase of the incident wave by a function $\varphi(x)$, the total phase change $\Psi(x)$ experienced by a wave traveling from point P, passing through the metasurface, and refracting to point Q can be expressed as:

$$\Psi(x) = \varphi(x) + \frac{2\pi}{\lambda_1}\sqrt{(x^2 - x_P^2) + y_P^2} + \frac{2\pi}{\lambda_2}\sqrt{(x^2 - x_Q^2) + y_Q^2} \#(1)$$

In the equation, λ_1 and λ_2 represent the wavelengths of the wave in medium 1 and medium 2, respectively. According to Fermat's principle, the path taken by a wave between two points is the one that results in an extremum (usually a minimum) of the optical path length. By taking the derivative of the above expression, the generalized Snell's law for refraction can be derived as [17]:

$$\frac{1}{\lambda_2}\sin\theta_i - \frac{1}{\lambda_1}\sin\theta_i = \frac{1}{2\pi}\frac{d\varphi(x)}{dx}\#(2)$$

Similarly, the generalized Snell's law for reflection can be expressed as:

$$\frac{1}{\lambda_1}\sin\theta_r - \frac{1}{\lambda_1}\sin\theta_i = \frac{1}{2\pi}\frac{d\varphi(x)}{dx}\#(3)$$

When the metasurface is composed of discontinuous subwavelength unit cells, the term $\frac{d\phi(x)}{dx}$ can be rewritten as $\frac{\Delta\phi}{\Delta x}$, which represents the phase gradient of the metasurface. Thus, when the medium remains unchanged, the incident wave will undergo refraction and reflection upon passing through the metasurface. The phase gradient of the metasurface determines the magnitudes of the refraction and reflection angles. Since $\frac{d\phi(x)}{dx}$ is a positive value, the refraction angle is always larger than the incident angle. When the refraction angle equals 90°, the refracted wave propagates parallel to the metasurface, and the corresponding incident angle is defined as the critical angle θ_c. From equation (2), when the media on both sides are identical, the critical angle can be expressed as:

$$\theta_c = \arcsin\left(1 - \frac{\lambda_1}{2\pi}\frac{\Delta\varphi}{\Delta x}\right)\#(4)$$

When the incident angle exceeds the critical angle, the incident wave no longer follows the generalized Snell's law upon interaction with the metasurface. Instead, higher-order diffracted waves are generated according to higher-order diffraction theory, which forms the theoretical basis for the subsequent discussion of asymmetric transmission phenomena.

2.2. Unit Cell Design

According to the generalized Snell's law, a metasurface capable of introducing phase variation can achieve precise control over the phase of elastic-waves. Therefore, the primary task is to design a subwavelength structure that can induce phase changes through either local resonance or space-coiling mechanisms. However, due to structural constraints, space-coiling metasurfaces require the redesign of the unit cell phase distribution for each specific function, prompting the exploration of actively tunable metasurfaces. Given the complexity of modulation within a single physical field, the introduction of multiphysics coupling for external control is considered. Among multiphysics coupling approaches such as magneto-mechanical, thermo-mechanical, and electromechanical coupling,
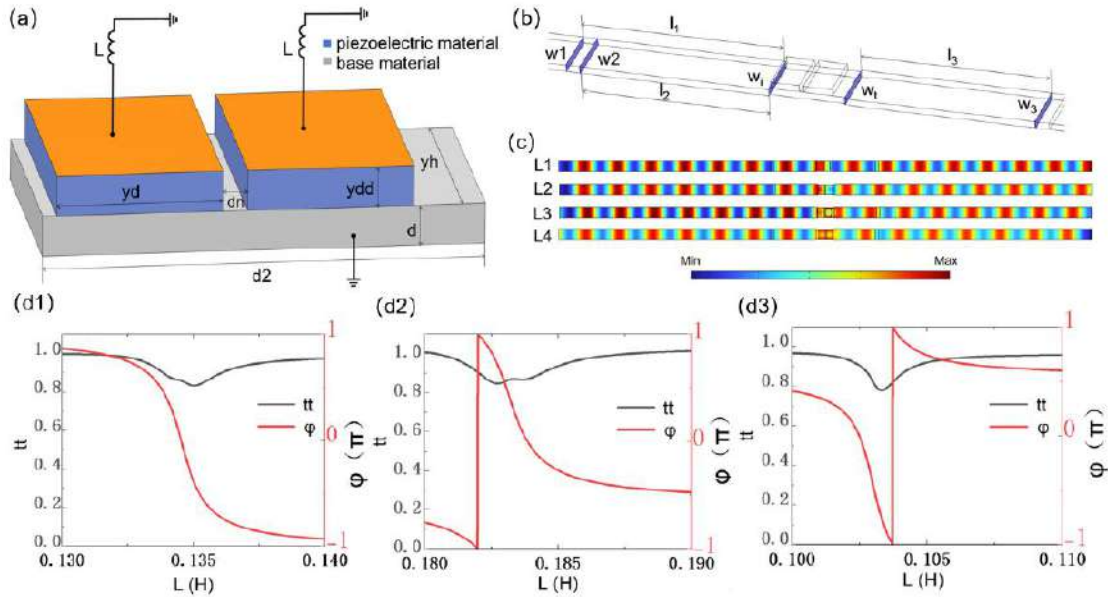
Figure 1: (**a**) Schematic diagram of the unit cell model. (**b**) Diagram of the model for calculating the transmission and reflection coefficients. (**c**) Displacement field plots corresponding to phase shifts of -π/2, 0, π/2, and π controlled by different inductances. (**d**) The transmission coefficient (black line) and phase shift (red line) as functions of the external inductance at frequencies of 14 kHz, 12 kHz, and 16 kHz, respectively.

electromechanical coupling stands out as the preferred choice due to its wide tunability and minimal external equipment requirements. One of the most typical electromechanical coupling materials is piezoelectric material.

Piezoelectric materials possess the ability to couple elastic deformation with electric field effects. By connecting piezoelectric materials to shunt circuits, external electrical signals can alter the electric field within the piezoelectric material, thereby modulating its elastic deformation. Shunt inductor circuits are commonly used with piezoelectric materials. The inductor in the circuit can form an electrical LC resonant system with the inherent capacitance of the piezoelectric material. When the system reaches the resonant frequency, the piezoelectric material undergoes strong resonance within the entire elastic structure, producing effects similar to those of a local resonant oscillator. Therefore, piezoelectric materials are also employed to design low-frequency band gaps in metamaterials. Compared to elastic structures with locally resonant metamaterials, piezoelectric metamaterials with shunt inductor circuits offer more predictable resonant band gaps, and their bandgap frequencies can be tuned by adjusting the components of the shunt circuit.

Based on these characteristics, a unit cell is designed using piezoelectric material with electromechanical coupling effects, as shown in Figure

1a. Only when the unit cell length d_2 is subwavelength can the modulated elastic waves achieve a good resolution. Given that the minimum wavelength is 29.8 mm at 16 kHz within the research scope of this paper, is selected to be 16 mm for better resolution. For the convenience of subsequent regulation of high-order diffracted elastic waves, the unit cell width should be less than half the wavelength (14.9 mm). On this basis, an appropriate size of the piezoelectric patch can be selected accordingly. Ultimately, the dimensions of the two piezoelectric patches are set as $y_h \times y_d \times y_{dd} = 9 \times 6 \times 1.5 \, \text{mm}^3$. The spacing between the two piezoelectric patches is denoted as the parameter d_n. A substrate material for elastic-wave transmission is set as $d_2 \times y_h \times d = 16 \times 9 \times 1.5 \, \text{mm}^3$. The first piezoelectric patch is positioned 0.5 mm from the left boundary of the unit cell, and d_n is optimized through parametric scanning to 0.9 mm. Shunt circuits are connected externally to the two piezoelectric patches. The bottom sides of both patches are grounded, while their top sides are connected to an externally tunable inductor, with the other end of the inductor also grounded, forming a simple LC oscillation circuit. When elastic-waves enter the unit cell, they resonate with the piezoelectric materials and the external circuit, resulting in phase changes [19].

To verify the authenticity of the phase changes, a test model is constructed in finite element simulation software for virtual experiments. High-density mesh

regions (l_2 and l_3) are established on both sides of the unit cell. The maximum size of the computational mesh elements must be less than 0.5 mm to ensure the accuracy of numerical calculations. Two cross-sections are selected on the left and right sides of these high-density mesh regions as interfaces for calculating the intensity and phase of the incident and transmitted waves (w_2 and w_3). The remaining parts serve as wave propagation zones for observing phase variations. Finally, perfectly matched layers (PML) are added on both sides to eliminate the effects of reflected waves. It is worth noting that the width of the wave propagation zones should be slightly larger than that of the unit cell (10 mm and 9 mm, respectively) to avoid mutual coupling interference when multiple unit cells are placed side by side to form the metasurface.

As shown in Figure **1b**, the displacements at the left and right boundaries of the unit cell, W_i and W_t, can be expressed as:

$$W_i = (W_I + W_R)e^{-i\omega t} \#(5)$$

$$W_t = W_T e^{-i\omega t} \#(6)$$

In the above equations, W_I, W_R, and W_T represent the displacement amplitudes of the incident, reflected, and transmitted waves, respectively.

Let the out-of-plane displacements at distances l_1 and l_2 from the left side of the unit cell be w_1 and w_2, and the out-of-plane displacement at distance l_3 from the right side be w_3. These can be obtained as:

$$w_1 = W_I e^{-ikl_1} + W_R e^{-ikl_1} \#(7)$$

$$w_2 = W_I e^{-ikl_2} + W_R e^{-ikl_2} \#(8)$$

$$w_3 = W_T e^{-ikl_3} \#(9)$$

Based on equations (7) to (9), the expressions for the reflection coefficient rr and transmission coefficient tt can be derived as[17]:

$$rr = \frac{W_R}{W_I} = \frac{w_2\, e^{-ikl_2} - w_1 e^{ik\,(l_1 - 2l_2)}}{w_1\, e^{ikl_1} - w_2 e^{ik\,(2l_1 - l_2)}} \#(10)$$

$$tt = \frac{W_T}{W_I} = \frac{w_3\, e^{-ikl_3}\left(1 - e^{i2k\,(l_1 - l_2)}\right)}{w_1\, e^{ikl_1} - w_2 e^{ik\,(2l_1 - l_2)}} \#(11)$$

Finally, the derived formulas and material properties are implemented in the COMSOL Multiphysics simulation software. The substrate material is 304 stainless steel, and the piezoelectric material is PZT-

5H. At a frequency of $f = 14\,kHz$, an excitation with a magnitude of $1 \times 10^{-7}\,N/m^2$ is applied on the left side. After configuring the external circuit, a parametric sweep of the shunt inductance L is performed to verify the unit cell's capability to modulate the phase of elastic-waves. The resulting transmission coefficient (tt) and phase shift (ϕ) are shown in Figure **1d1**. It can be observed that the phase variation ranges approximately from -3 to 3, which is attributed to the relatively narrow sweep range of L. Observing the phase variation over a broader range of L would reveal that it satisfies the phase coverage requirement from $-\pi$ to π. Examining the transmission coefficient curve (black line), it is evident that when the phase undergoes significant changes, the corresponding transmission coefficient drops notably. This is because the resonant interaction between the shunt inductor and the capacitance of the piezoelectric patches significantly alters the effective stiffness of the structure. Consequently, as the system approaches the resonant peak, the change in effective stiffness becomes more pronounced and the influence on the wave phase will be greater. Moreover, owing to the resonant effect of the electric circuit, the elastic energy of the structure is converted into the electric potential energy of the circuit, which leads to a larger energy loss of elastic waves. However, as long as the transmissivity is higher than 0.75, the transmitted energy will exceed 0.5, and thus the proposed model remains valid in theory.

2.3. Verification of Unit Cell Tunability

After completing the unit cell modeling, the displacement field plots were examined to validate its tunability. Four external inductance values, L1, L2, L3, and L4, corresponding to phase shifts of -π/2, 0, π/2, and π, were selected. The displacement field plots of the unit cell under these corresponding parameters were observed and compared, as shown in Figure **1c**. The results indicate that the phase of the incident wave on the left side remains nearly consistent. After adjusting the external inductance, the phase of the transmitted wave on the right side changes, while its amplitude remains sufficiently high. This demonstrates that the designed unit cell can effectively modulate the phase of the transmitted wave while maintaining a high transmission coefficient.

The tunability of the piezoelectric unit cell is reflected not only in its ability to achieve different phase shifts within the same cell but also in its capacity for phase modulation at different frequencies. To verify this

multi-frequency modulation capability and provide essential data for subsequent simulation experiments, the unit cell's ability to modulate the phase of elastic-waves was calculated at 12 kHz and 16 kHz without altering the model. It is important to note that when the frequency changes, the wavelength of the elastic-wave also varies. The wavelengths at 12 kHz and 16 kHz are 34.5 mm and 29.8 mm, respectively. The transmission coefficient and phase shift at these frequencies are shown in Figures **1d2** and **1d3**. It can be observed that at 12 kHz, as L varies within the range of 0.18 H to 0.19 H, the phase changes continuously and approximately covers the range from -π to π. The incomplete coverage is again due to an insufficient parameter sweep range. The transmission coefficient remains within a high range above 0.85, showing better performance compared to the results at 14 kHz. At 16 kHz, the phase shift, represented by the red line, also falls within the -π to π range. However, the transmission coefficient in this case drops to a minimum of 0.77. Although this value remains above 0.75 and is still usable, potential adverse effects on the simulation results should be noted.

3. TUNABLE ELASTIC METASURFACE

3.1. Metasurface Simulation Model

A single unit cell can only alter the phase of an elastic-wave. To control the propagation direction of elastic-waves, a metasurface composed of multiple unit cells is required. Therefore, it is necessary to first complete the modeling of a tunable piezoelectric metasurface. A model as shown in Figure **2a** is established. The blue outer ring represents the perfectly matched layer (PML), used to eliminate interference from reflections at the boundaries. The red surface on the left is the excitation interface for a Gaussian beam, capable of generating Gaussian beams with arbitrary width and incident angle. The central part is the metasurface composed of 24 unit cells arranged side-by-side.

To generate a tunable Gaussian beam, a function expression *fw* is introduced in COMSOL:

$$fw(y) = A \times e^{\frac{-(y - p \times h)^2}{c}} \#(12)$$

In this equation, *A* is the amplitude of the Gaussian wave, set here to 1×10^{-7}; h is the total length of the
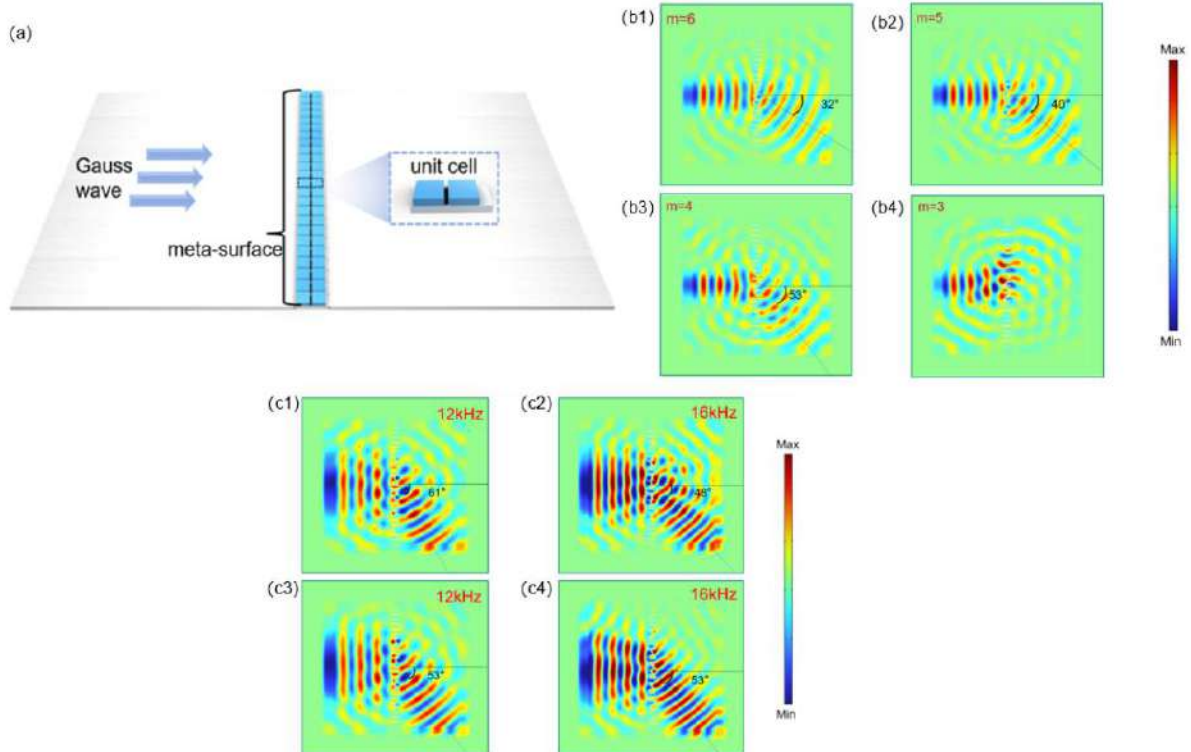
Figure 2: (**a**) Schematic of the metasurface simulation model. (**b**) Displacement field plots of metasurface-controlled elastic-wave refraction for the number of unit cells in a supercell m equal to 6, 5, 4, and 3, respectively. The corresponding theoretical refraction angles are 32°, 40°, 53°, and non-existent. (**c1**) (**c2**) When the frequency changes to 12 kHz and 16 kHz while keeping m = 4, the refraction angle changes accordingly. (**c3**) (**c4**) By adjusting the phase gradient, the refraction angle remains unchanged despite variations in frequency.

excitation interface; p is the ratio of the Gaussian beam generation height to the total length, used to control the vertical position where the Gaussian beam originates; and c controls the width of the Gaussian beam. Building on this, an angle control factor is added:

$$Fw = fw(y) \times e^{i \times k \times y \times \sin(\theta_i)} \#(13)$$

Here, k is the angular wavenumber, representing the phase change in radians per unit length, with a value of $2\pi/\lambda$. θ_i is the incident angle. Thus, by modifying the values of p and θ_i, Gaussian beams can be generated at arbitrary positions and angles.

$$\theta_t = \arcsin\left(\frac{\lambda}{2\pi}\frac{\Delta\varphi}{\Delta x}\right) \#(14)$$

3.2. Tunable Elastic-Wave Refraction

According to the generalized Snell's law, the phase gradient within a metasurface causes elastic-waves to refract. When the incident angle is fixed, the sine of the refraction angle exhibits a linear relationship with the phase gradient. Therefore, fundamental refraction phenomena will be used to verify the correctness of the previous work. First, the concept of a supercell is introduced. A supercell consists of m unit cells with uniformly varying transmission phases. The metasurface is then composed of n supercells arranged in a repeating pattern. If the width of a single unit cell is *L*, the total width of the metasurface is $m \times n \times L$, and the phase gradient is $2\pi/(mL)$. Based on Equation (3), assuming identical media on both sides of the metasurface, a discontinuous phase change, and an incident angle of 0 degrees, the formula for calculating the refraction angle becomes:

$$\theta_t = \arcsin\left(\frac{\lambda}{2\pi}\frac{\Delta\varphi}{\Delta x}\right) \#(15)$$

$\Delta\varphi/\Delta x$ is determined by the number of unit cells m within a supercell. First, a simulation is conducted with m = 4. Under this configuration, the phases of the unit cells within the supercell are -π/2, 0, π/2, and π, respectively. The calculated wavelength for 304 stainless steel at 14 kHz is 31.9 mm. According to Equation (12), the theoretical refraction angle is calculated to be 53 degrees. The simulation results are shown in Figure **2b3**. Observation of the results reveals that the incident wave behaves as expected, entering from the left at 0°. After passing through the central metasurface, it undergoes a significant angular deflection. The figure indicates a theoretical deflection angle of 53°, which aligns with the central axis of the

refracted wave's waveform, confirming that the refracted wave propagates along the theoretically predicted angle. It is worth noting that the amplitude of the refracted wave is slightly smaller than that of the incident wave, possibly due to less-than-unity transmission through the unit cells. Additionally, a slight divergence trend in the refracted wave can be observed. This is likely because the incident beam is relatively narrow, spanning only 5 unit cells in width. According to Huygens' principle, each wave transmitted from a unit cell can be considered a new source, leading to a slight divergence. The high degree of agreement between the simulation and theory validates the correctness of the unit cell and metasurface simulation.

Building on the above, and leveraging the superior tunability of the piezoelectric metasurface, different refraction angles at the same frequency are achieved without altering any part of the model, only by changing the external inductance values to adjust m. Simulations are conducted for m = 3, m = 5, and m = 6, preceded by theoretical analysis. Calculations show that for m = 5 and m = 6, the theoretical refraction angles are 40° and 32°, respectively. The simulation results are shown in Figures **2b2** and **2b1**. The central axis of the refracted wave's waveform closely aligns with the theoretical refraction angle lines, demonstrating good agreement between simulation and theory and confirming the metasurface's excellent angular control performance. Meanwhile, for m = 3, the calculated value of sinθt exceeds 1, indicating no valid refraction angle exists. This is also verified by the simulation result shown in Figure **2b4**, providing further evidence for the correctness of the method.

During the unit cell design phase, it was verified that the unit cell can modulate elastic-waves at different frequencies. Therefore, the metasurface should also be capable of controlling wave refraction across different frequencies. For most passive unit cells, the value of m is fixed. When the frequency changes to 12 kHz and 16 kHz, the elastic-wavelength becomes 34.5 mm and 29.8 mm, respectively. Consequently, for most metasurfaces with fixed phase profiles, even if they are adaptable to multiple frequencies, the refraction angle would change to 61° and 48° respectively due to the wavelength change. However, benefiting from the arbitrarily tunable phase of its unit cells, the piezoelectric metasurface can achieve any desired phase gradient. Therefore, when the frequency changes, the refraction angle can either change accordingly or remain the same as before. Based on

the phase-inductance correspondence table established during unit cell construction, inductance values corresponding to the required phases were selected for simulation.

Figures **2c1** and **c2** show the refraction images of the metasurface for m=4 at 12 kHz and 16 kHz, respectively. Here, the refraction angle changes, and the figures show the corresponding theoretical angles. Subsequently, the phase gradient was adjusted to maintain the refraction angle at 53° for simulations at these frequencies. The calculated required phase gradients for 12 kHz and 16 kHz are 0.145 rad/mm and 0.168 rad/mm, respectively. The phase distribution across the metasurface was determined accordingly, and the simulation results are shown in Figures **2c3** and **c4**. The transmitted waves propagate along the theoretically predicted directions. Comparing the upper and lower figures, it can be observed that adjusting the phase gradient effectively corrects the impact of wavelength change on the transmission angle. These simulations collectively prove that the piezoelectric metasurface retains the capability to control the refraction angle of elastic-waves within the frequency range of 12 kHz to 16 kHz.

3.3. Tunable Subwavelength Focusing of Elastic-Wave

Similar to how a triangular glass prism refracts light while a convex lens focuses parallel light beams, one can consider whether a metasurface with a non-uniform phase profile can also focus parallel incident elastic-waves at a single point by varying the refraction angle at different positions. To achieve focus at point (f, 0), the refraction angle θ_t at point A located in the metasurface with a vertical coordinate y should satisfy the following. According to the generalized Snell's law:

$$\sin\theta_t = \frac{\lambda}{2\pi}\frac{\Delta\varphi}{\Delta x}\#(16)$$

From geometric relations, we have:

$$\sin\theta_t = \frac{y}{\sqrt{y^2 + f^2}}\#(17)$$

Combining these equations yields the expression for phase variation with respect to y [17]:

$$\varphi(y) = \frac{2\pi}{\lambda}\left(\sqrt{y^2 + f^2} - f\right)\#(18)$$

Equation (18) can be used to calculate the required phase for each of the 24 unit cells and their corresponding inductance values. Based on this theory, a simulation model was constructed. The parameter *c* in the Gaussian beam definition was increased to generate a sufficiently wide incident elastic-wave, simulating a parallel beam. Since energy is proportional to the square of the amplitude, the square of the amplitude field is used as an approximation for the energy field. The resulting approximate energy field is shown in Figure **3a**. For comparison, after removing the gaps between unit cells and eliminating the piezoelectric materials, an approximate energy field plot for wave propagation *without* the metasurface focusing effect was obtained, as shown in Figure **3b**. Both plots share a unified color axis, allowing direct comparison of energy distribution via color observation.

The incident wave approximates a parallel beam. As observed, the tunable piezoelectric metasurface demonstrates a significant subwavelength focusing effect on the elastic-wave, with the focal region appearing elliptical. Some weaker energy concentration points are also present on either side in front of the main focal point. In contrast, the Gaussian wave propagating without the metasurface shows no distinct
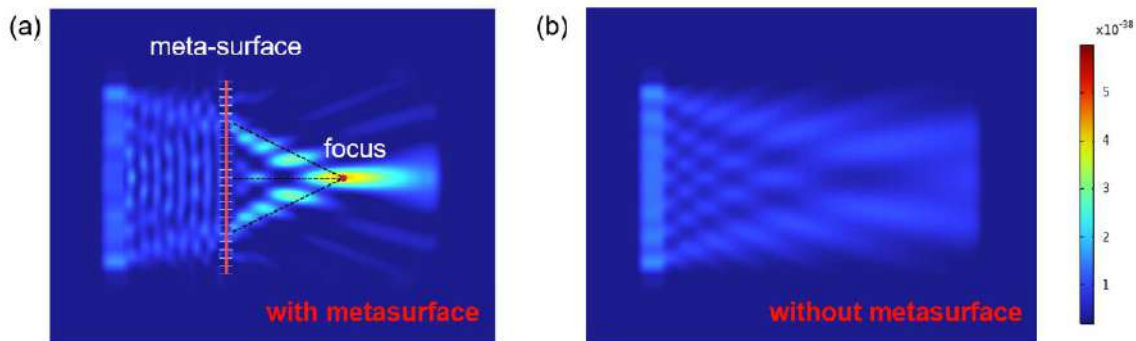
Figure 3: (**a**) Approximate energy field diagram of elastic-wave subwavelength focusing with a focal length of 120 mm achieved by the piezoelectric metasurface. (**b**) Approximate energy field diagram of elastic-wave propagation without the influence of the metasurface.

focal point and exhibits approximately parallel propagation.

A line was taken along the central axis of the plate surface at y=0, z=0 to study the variation of the ratio R (the elastic-wave energy normalized by the maximum energy) after the wave exits the metasurface. The energy distribution plot indicates that the actual focal position is approximately 140 mm. The energy variation is more gradual after the focal point compared to before it, explaining the elliptical shape of the focal region observed in Figure **3a**. Introducing the relative error calculation formula $\frac{f-f_0}{f_0}$, the computed relative error is 6.6%, which is within an acceptable range.

Building upon this, the tunability of the piezoelectric metasurface regarding the subwavelength focusing effect is further investigated. It is first noted that lenses of different thicknesses can focus light at different positions. By analogy, metasurfaces with varying phase profiles should theoretically also be capable of focusing elastic-waves at different focal points. Given the advantage of the piezoelectric metasurface, which requires only the adjustment of external parameters, it is theoretically possible to control the focal point without altering the physical model. The theoretical focal points are first set to 100 mm and 80 mm. Using Equation (18), the required phase shift for each unit cell position can be determined. Subsequently, by adjusting the corresponding inductance values, the model is

modified accordingly. The resulting effects are illustrated in Figures **4a** and **b**.

The actual focal positions are located at 86 mm and 66 mm, respectively. Calculating the relative errors for the intended 100 mm and 80 mm focal points yields 14% and 17.5%. It can be observed that the shorter the focal length and the closer the focal point is to the metasurface, the larger the error becomes. A possible reason for this trend is that a smaller focal length requires more drastic phase changes between adjacent unit cells. In such cases, the drawback of discontinuous phase variation across the metasurface becomes increasingly amplified, leading to more significant errors.

Similar to the tunable refraction of elastic-waves, the superior adaptability of the tunable piezoelectric metasurface is further verified by achieving focusing at the same position across different frequencies. Setting the target focal point at 100 mm, the corresponding inductance distributions are determined for each frequency, and data simulations are performed. The results are shown in Figures **4c** and **d**. The figures demonstrate that, besides 14 kHz, the piezoelectric metasurface also exhibits excellent focusing capabilities at 12 kHz and 16 kHz, with the focal regions maintaining an elliptical shape. This validates the multi-frequency focusing ability of the tunable
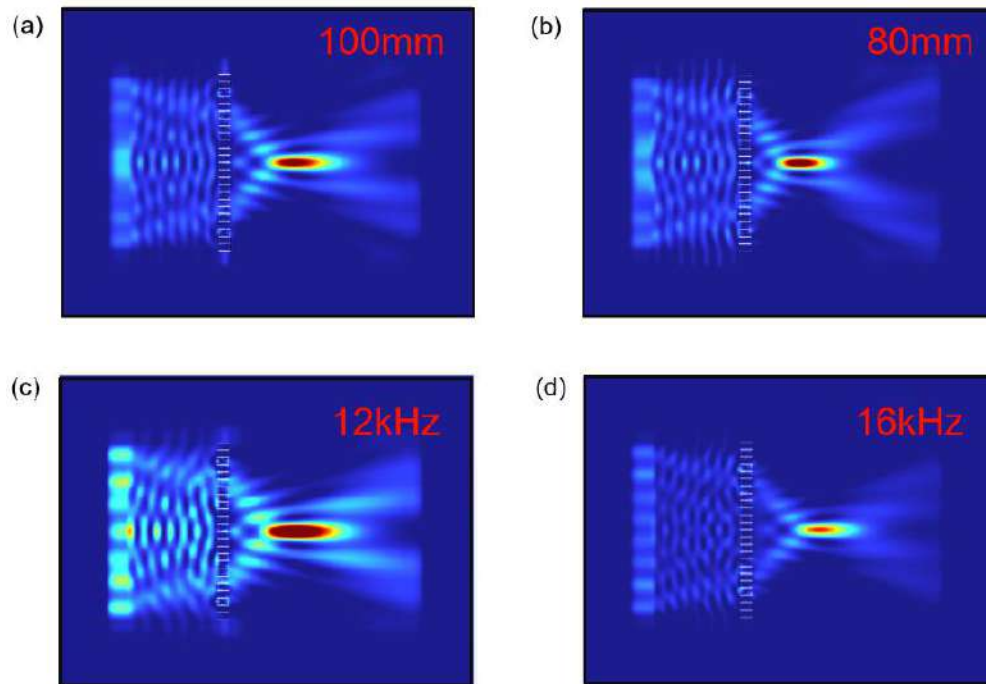
Figure 4: (**a**) (**b**) Approximate energy field diagrams at 14 kHz showing focal lengths adjusted to 100 mm and 80 mm, respectively, by only changing the external inductance parameters. (**c**) (**d**) Approximate energy field diagrams with a fixed focal length of 100 mm when the frequency is changed to 12 kHz and 16 kHz, respectively.

piezoelectric metasurface. Following the same method as before, cross-sectional lines are selected. The actual focal positions at 12 kHz and 16 kHz are found to be 86.2 mm and 91.7 mm, respectively. The corresponding relative errors are calculated to be 13.8% and 8.3%. Observing the pattern of errors reveals that all focal points are located slightly forward of the theoretical positions. This may be partly attributed to the inherent slight converging tendency of the incident wave itself. Another contributing factor could be that at 12 kHz and 14 kHz, the wavelength is less than twice the unit cell length, potentially compromising the subwavelength focusing effect. In contrast, at 16 kHz, the wavelength exceeds twice the unit cell length, leading to a better subwavelength focusing performance.

3.4. Wave Source Illusion

Elastic-wave cloaks based on transformation methods or designed using metamaterials/ metasurfaces have already been demonstrated. However, due to the form-invariance of elastodynamic equations and the complexity of passive metasurface structures, the resulting cloaks often lack tunability and cannot adapt to diverse requirements. Therefore, research in this area continues to face significant challenges. The tunable piezoelectric unit cell designed earlier offers a novel approach to addressing this issue. By leveraging the phase modulation capability of the piezoelectric unit cell, not only can wave source illusion effects be achieved, but the adjustable phase also implies the potential for arbitrary positioning of the illusory source and adaptability across multiple frequencies.

First, a ring-shaped metasurface model is constructed, as shown in Figure **5a**. The red circular ring represents the metasurface. The wave source at point O generates a cylindrical wave. After propagating a certain distance, the wave encounters the ring-shaped metasurface composed of 36 unit cells. At this interface, the phase of the propagating wave is altered, and it is subsequently projected with a new propagation pattern. After passing through an observation region, the wave is finally absorbed by a perfectly matched layer. The principle behind the wave source illusion effect is briefly explained here. The cylindrical wave generated by the point source at O is refracted upon passing through the metasurface, resulting in a cylindrical wave field that appears to originate from a new center O'. This creates the illusion of a shifted source. If the displacement distance of the wave

source is Δx, the unit cell position is θi, the refraction angle is -θ, and the radius of the metasurface is R, the geometric relationship yields:

$$R_m = \sqrt{(Rcos\theta i + \Delta x)^2 + (Rsin\theta i)^2} \#(19)$$

Combining the sine theorem and the generalized Snell's law, we obtain:

$$\frac{d\phi}{d\theta i} = \frac{-2\pi}{\lambda}\frac{R\Delta x sin\theta i}{Rm}\#(20)$$

Integrating the above expression gives[19]:

$$\phi(\theta i) = \frac{2\pi}{\lambda}(Rm - R)\#(21)$$

Using equations (19) and (21), the required phase for each unit cell at different positions can be calculated. First, the offset distance Δx is set to 10 mm. After calculating the corresponding phase distribution and configuring the phase parameters for each unit cell, a data simulation is performed. The result is shown in Figure **5b1**. In the figure, the small red circle indicates the actual position of the wave source, while the small white circle represents the position of the "illusory" wave source corresponding to the cylindrical wave transmitted through the metasurface. Δx denotes the horizontal coordinate difference between the two sources, i.e., the actual offset distance. The large red circle represents the outer boundary of the metasurface, centered on the actual wave source. The black dashed lines indicate the propagation contours of the transmitted waves with equal phase. The figure shows that the elastic-wave field after passing through the ring-shaped metasurface remains a cylindrical wave. Comparing the large red circle with the black dashed lines reveals that the center of the black dashed lines is offset relative to the point source position. The measured offset distance is Δx = 8.8 mm, with a relative error of approximately 12%, which is generally consistent with theoretical predictions. This demonstrates that source displacement can be achieved through phase design of the ring-shaped metasurface.

Simultaneously, to verify the tunability of the piezoelectric metasurface, the theoretical offset distance is set to -25 mm. The phase distribution is recalculated accordingly, and only the external parameters are modified for the simulation. The result is shown in Figure **5b2**. It can be observed that the direction of the source shift changes, and the magnitude of the shift increases, aligning with the
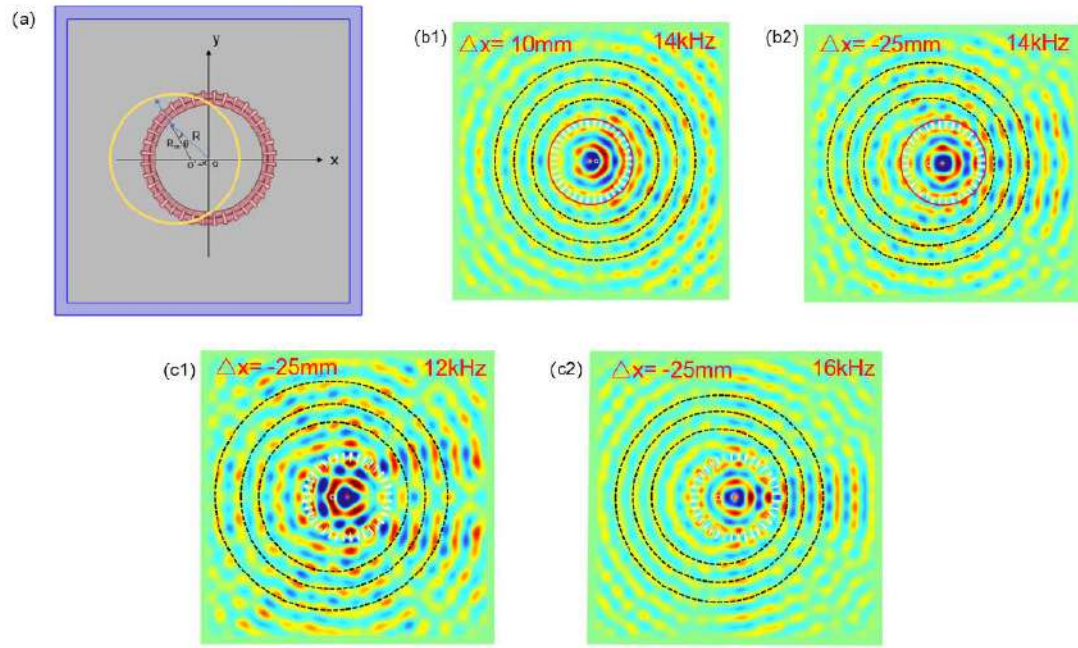
Figure 5: (**a**) Schematic diagram illustrating the principle of generating an illusionary wave source. (**b1**) (**b2**) Displacement field plots of the metasurface at 14 kHz when the displacements of the illusionary wave source are set to 10 mm and -25 mm, respectively. The red small circle indicates the actual wave source, while the white small circle denotes the illusionary source. (**c1**) (**c2**) Displacement field plots of the metasurface generating an illusionary source with a displacement of -25 mm when the frequency is changed to 12 kHz and 16 kHz, respectively.

theoretical offset distance of -25 mm. Specifically, the calculated offset distance is Δx = -27.1 mm, with a relative error of 8.4%.

Building on this, the frequency adaptability of the tunable piezoelectric metasurface is further examined. At 12 kHz and 16 kHz, due to changes in the elastic-wavelength, the required phase variations at each position are recalculated. After adjusting the corresponding external parameters, data simulations are conducted, with results shown in Figures **5c1** and **c2**. The results indicate that the ring-shaped metasurface effectively produces virtual displacement of the point source at both 12 kHz and 16 kHz. The measured offset distances at 12 kHz and 16 kHz are -26.8 mm and -27.9 mm, with relative errors of 7.2% and 11.6%, respectively, which are within an acceptable range.

4. A SYMMETRIC TRANSMISSION

The phenomenon of asymmetric transmission refers to the situation where an incident wave is blocked when propagating from one direction but transmits normally when incident from the opposite direction[20-22]. This phenomenon enhances flexibility in controlling the direction of wave energy propagation. Extensive research has been conducted on asymmetric transmission for electromagnetic and acoustic waves

[23-27]. In current studies, the acoustics field has achieved significant attenuation of diffracted wave energy by utilizing multiple reflections of higher-order diffracted waves and incorporating loss into metasurfaces. Lower-order modal waves, lacking multiple reflections, are less affected by such losses. By designing metasurfaces to generate different modal diffracted waves for waves incident from opposite directions, asymmetric acoustic transmission has been realized. However, research on asymmetric transmission in the field of elastic-waves remains scarce.

Although introducing loss into metasurfaces can achieve relatively pronounced asymmetric phenomena, it also brings several issues. First, the strength of asymmetry is related to the magnitude of the introduced loss, and finding the optimal loss factor for the best asymmetric performance is challenging to quantify experimentally. Second, while adjusting loss can create asymmetry, the presence of loss inevitably attenuates the wave energy even in the desired transmission direction. Therefore, achieving asymmetric elastic-wave transmission using a lossless single-layer metasurface while maintaining high transmission efficiency at the desired output port remains a significant challenge in the field of asymmetric elastic-wave control. To address this

problem, this chapter will delve into the existing theory of higher-order diffraction. Based on this theory, new design methods and strategies will be proposed to realize asymmetric elastic-wave transmission using a single-layer lossless metasurface. Theoretical calculations and numerical simulations will be conducted to analyze its asymmetric characteristics.

4.1. Theory of Higher-Order Diffraction

Higher-order diffraction theory first emerged in the field of electromagnetic wave research. When an electromagnetic wave (e.g., light) is incident on a planar periodic structure, higher-order diffraction may occur. In this case, the light not only reflects and refracts but also scatters into multiple distinct directions, a phenomenon known as diffraction orders. In recent years, with the rise of metasurface research, many scholars have incorporated higher-order diffraction theory into the design of metasurfaces and metamaterials, achieving various novel phenomena [28-30]. Furthermore, higher-order diffraction theory has been widely applied in the field of elastic-wave manipulation [31]. As introduced earlier, the critical angle θ_c defines a boundary: when the incident angle is less than θ_c, the incident and transmitted waves satisfy the generalized Snell's law, resulting in transmission; as the incident angle increases and approaches θ_c, the transmission angle also increases, eventually leading to propagation along the metasurface surface, with the transmitted wave converting from a propagating mode to a surface mode. When the incident angle exceeds the critical angle, higher-order diffracted waves are generated. Under this condition, the generalized Snell's law is no longer applicable and is replaced by formulas governing the various modal diffracted waves [11].

$$\sin\theta_t = \sin\theta_i + n\frac{\lambda}{2\pi}\frac{d\varphi(x)}{dx}\#(22)$$

When higher-order diffracted waves are generated, multiple reflections occur within the metasurface. After entering the metasurface, the elastic-wave reflects back and forth between its two boundaries. Following these multiple reflections, the elastic-wave may either transmit through or reflect back, becoming the transmitted or reflected wave, respectively. As shown in Figure **6a**, an incident orange wave is partially transmitted (depicted as the yellow wave) after undergoing 5 multiple reflections, while another portion is ultimately reflected (the red wave) after 8 multiple reflections.

Let the diffraction order of the higher-order diffracted wave be denoted by n. In general, n can be any integer. However, for cases where n>1, if the n-th order diffraction satisfies the corresponding equation, the generalized Snell's law still holds. Since wave diffraction tends to follow the propagation path with the shortest optical length, the wave propagates according to the generalized Snell's law in such scenarios. Therefore, diffraction orders with n>1 can be neglected. The possible values for n are 1, 0, -1, -2, ..., -λ, where -λ is the highest diffraction order. The case n=1 corresponds to the generalized Snell's law.

Denote the number of multiple reflections as L. For a supercell consisting of m unit cells with a phase difference of $2\pi/m$ between adjacent cells, after L reflections, the phase difference between adjacent unit cells becomes $L \cdot 2\pi/m$. Concurrently, the phase difference for a higher-order diffracted wave of order n between two adjacent unit cells is $n \cdot 2\pi/m$. Since adding or subtracting 2π does not change the physical meaning of the phase difference, the following equation can be established:

$$n\frac{2\pi}{m} + 2\pi = L\frac{2\pi}{m}\#(23)$$

Simplifying gives:

$$L = m + n\#(24)$$

It can be seen that the sum of the number of unit cells m in the supercell and the diffraction order n jointly determines whether the elastic-wave of that diffraction order ultimately transmits or reflects. When L is an even number, the incident wave is ultimately reflected back after multiple reflections. When L is an odd number, the incident wave transmits through after undergoing multiple reflections. When the diffraction order n to be controlled is determined, the only parameter deciding its transmission or reflection is m, i.e., the number of unit cells in the supercell.

4.2. Principle of Asymmetry and Supercell Simulation

Generally, when incident waves symmetric about the normal direction of a metasurface undergo modulation by the metasurface, resulting in diffraction waves that are no longer symmetric, this situation is referred to as asymmetric wave transmission. The propagation direction of the transmitted or reflected waves can be determined by the following formula [11]:

$$\sin\theta_{out} = \sin\theta_{in} + n\frac{\lambda}{S}\#(25)$$

where $S = m \times \Delta x$ is the width of the supercell. For an incident wave, when excessively high diffraction orders exist, some modal diffracted waves are reflected back, while others are transmitted. Since the transmission or reflection angles differ for different diffraction orders, this can lead to chaotic waveforms and obscure the observed phenomena. Therefore, it is necessary to minimize the presence of higher-order waves. Given that the 0th-order wave is typically weak, the goal is to at least control the emergence of the -1st order diffracted wave. In summary, we attempt to design a metasurface that produces only ±1st and 0th order waves during modulation. Considering the condition $-2 < \sin \theta_{\text{out}} - \sin \theta_{\text{in}} < 2$, the corresponding supercell of the metasurface should satisfy:

$$1 < \frac{\lambda}{S} < 2 \#(26)$$

Here, we consider a special case of generalized asymmetric transmission: two incident waves, after modulation by the metasurface, result in the negative-angle incident wave transmitting through the metasurface, while the positive-angle incident wave is reflected by it. The corresponding equations are:

$$\sin(-\theta_{\text{in}}) + n_1 \frac{\lambda}{S} = \sin\theta_r \#(27)$$

$$\sin(+\theta_{\text{in}}) + n_2 \frac{\lambda}{S} = \sin(-\theta_t) \#(28)$$

Since only +1, -1, and 0 order diffraction exist in the metasurface, the diffraction order n_1 for the negative-angle incident wave in Eq. (27) is 1, and n_2 for the positive-angle incident wave in Eq. (28) is -1. In this scenario, the two incident waves remain symmetric about the axis, and the angles of their transmitted and reflected waves are also numerically symmetric. As the negative-angle incident wave transmits through the metasurface following the generalized Snell's law, and according to Eq. (24), $L = m + n = m - 1$ should be an even number to ensure the positive-angle incident wave is reflected by the metasurface. Combining this with Eq. (26), we select $m = 3$ for asymmetric data simulation. For an Ao-mode elastic-wave at 14 kHz, the ratio $\lambda/S = 31.9/30 = 1.06$ satisfies the requirement of Eq. (26). The calculated critical angle for +1 order diffraction is $\theta_C = -3.4°$. Therefore, the positive and negative incident angles should be greater than 3.4° and less than $-3.4°$, respectively.

Given the complexity of the asymmetric phenomenon and the high computational cost associated with full metasurface simulation, we first construct a supercell model with $m = 3$ for preliminary simulation and debugging. The model is built by placing three unit cells side by side. Since this simulation requires observing the direction and magnitude of the reflected wave, and conventional simulations typically yield images showing the superimposed state of incident and reflected waves, we consider setting up a
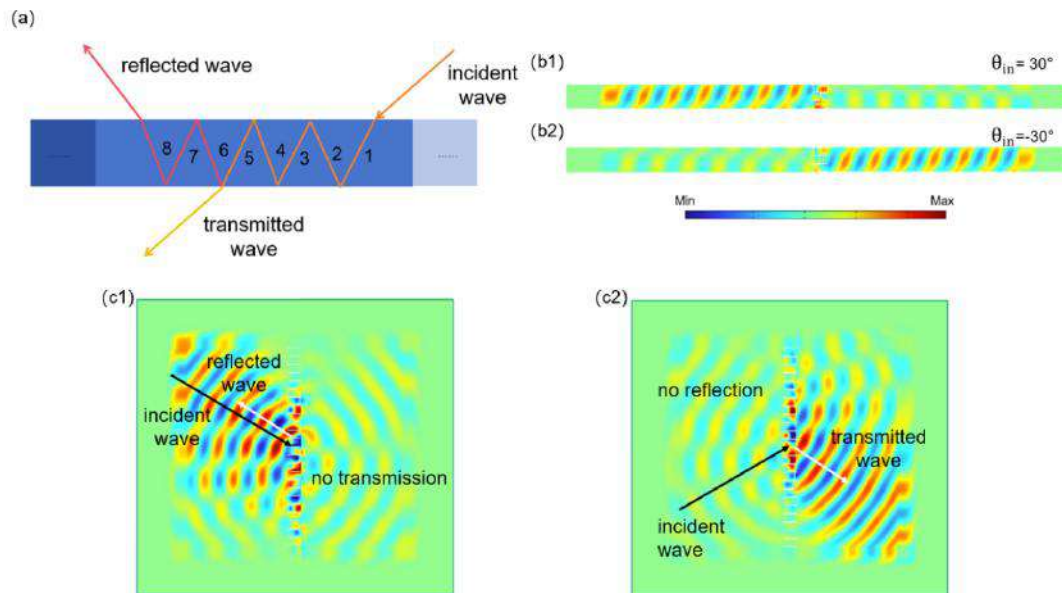
Figure 6: (**a**) Schematic diagram of the multiple reflection phenomenon in higher-order diffraction. (**b1**) (**b2**) Combined transmission and reflection displacement field diagrams for a supercell with m=3, with incidence angles of 30° and -30°, respectively. (**c1**) (**c2**) Combined transmission and reflection displacement field diagrams using the metasurface model from Chapter 3, with incidence angles of 30° and -30°, respectively. The black line indicates the direction of the incident wave, and the white line indicates the direction of the transmitted or reflected wave.

control experiment group. By filling the gaps between unit cells, removing the piezoelectric patches, and applying the same excitation, we obtain an auxiliary control group. Subtracting the displacement field of the control group from the original results yields a clean image of the reflected wave displacement field.

For an incident angle of $30°$, which is greater than the critical angle, higher-order diffraction occurs. Here, the -1 order wave dominates. With $m + n = 2$, the -1 order wave is reflected, and its reflection angle calculated by Eq. (28) is $-34°$. For an incident angle of $-30°$, which is less than the critical angle, higher-order diffraction does not occur. According to the generalized Snell's law, the elastic-wave transmits through, with a calculated transmission angle of $34°$. After setting the inductance values, periodic conditions, and angles to $\pm30°$, the simulation is run. The resulting transmission and reflection fields are combined, as shown in Figures **6b1** and **b2**. Figure **b1** displays the transmission and reflection fields for a $30°$ incidence, where the transmitted wave energy is nearly zero, and a reflected wave with an angle close to the incident angle is generated. Figure **b2** shows the results for a $-30°$ incidence, where a transmitted wave approximately opposite to the incident angle is produced, and the reflected wave intensity is almost zero. The simulation results align well with the theory, confirming the reliability of the simulation.

4.3. A Symmetric Propagation

After debugging the parameters and successfully achieving asymmetric transmission in the supercell, eight supercells were arranged in a repeating pattern to form a metasurface with m=3*. Leveraging the advantage of external tunability of the piezoelectric metasurface, the metasurface model from Chapter 3 could still be used, requiring only changes to the external inductance parameters and the Gaussian wave incidence conditions. Similar to the supercell case, a control group was set up to observe the reflected wave. For Gaussian waves incident at ±30 degrees, the combined images of the transmission and reflection fields are shown in Figures **6c1** and **c2**, respectively. Similar to the phenomena observed in the supercell, when the wave is incident at a positive angle (Figure **c1**), the transmitted wave intensity is nearly zero, with only some scattered waves passing through. The reflected wave, dominated by the -1st order higher-order wave, generates a reflection propagating opposite to the incident direction (back along the original path), consistent with the calculated reflection angle of -34°. When the wave is incident at a negative angle (Figure **c2**), no higher-order diffraction occurs, and thus no reflected wave is present. According to the generalized Snell's law, a transmitted wave propagating opposite to the incident direction is generated, consistent with the calculated 34° result. The phenomena in the full metasurface, lacking periodic boundary conditions and offering a larger observation area, are more convincing and pronounced compared to those in the single supercell.

5. CONCLUSIONS

Addressing the need for active tunability of elastic-waves using metasurfaces, this work has established a robust framework for the design of piezoelectric metasurfaces. Progressing from unit cell design to metasurface construction, the theoretical foundations and numerical simulations for tunable elastic-wave control have been explored. By integrating piezoelectric unit cells with external inductive shunts, we achieved full 2π phase modulation and dynamic frequency tunability without requiring structural modifications. This electromechanical control enabled a suite of exotic elastic-wave phenomena, including tunable anomalous refraction and subwavelength focusing, effectively realizing the elastic equivalent of an optical zoom lens. Furthermore, we demonstrated the versatility of this approach by constructing a ring-shaped metasurface capable of generating elastic-wave source illusions. We extended the operational framework beyond the conventional generalized Snell's law by harnessing higher-order diffraction modes. This allowed us to realize switchable asymmetric transmission, where the metasurface exhibits high transmittance in one direction and near-total reflection in the other. These findings not only validate the theoretical potential of higher-order diffracted waves but also provide a practical pathway for the next generation of intelligent structural systems. By offering precise, real-time control over multimodal wave propagation, this platform paves the way for advanced applications in vibration isolation, energy harvesting, and smart structural health monitoring.

ACKNOWLEDGEMENTS

REFERENCES

[1]   Cawley P. Guided waves in long range nondestructive testing and structural health monitoring: Principles, history of applications and prospects. NDT & E International 2024; 142: 103026.

[2]   Ricci F, Monaco E, Boffa N, Maio L, Memmolo. Guided waves for structural health monitoring in composites: A review and implementation strategies. Prog Aeosp Sci 2022; 129: 21. https://doi.org/10.1016/j.paerosci.2021.100790

[3]   Hu Y, Li Y, Liu Y, Li B, Christensen J. Giant elastic-wave asymmetry in a linear passive circulator. Nat Commun 2025; 16(1): 10. https://doi.org/10.1038/s41467-025-59313-0

[4]   Yang Z, Yi J, Li F, Li Z, Ye L, Li B, *et al*. Static mechanical cloaking and camouflage from disorder. Nat Commun 2025; 16(1): 12. https://doi.org/10.1038/s41467-025-63939-5

[5]   Cao L, Yang Z, Xu Y, Fan S, Zhu Y, Chen Z, *et al*. Flexural wave absorption by lossy gradient elastic metasurface. J Mech Phys Solids 2020; 143: 23. https://doi.org/10.1016/j.jmps.2020.104052

[6]   Wang W, Iglesias J, Jin Y, Djafari-Rouhani B, Khelif A. Experimental realization of a pillared metasurface for flexural wave focusing. APL Mater 2021; 9(5): 7. https://doi.org/10.1063/5.0052278

[7]   Jiang Y, Liu Y, Kou M, Li H, Wu X, Zeng X, *et al*. Multi-parameter independent manipulation for flexural wave by notched metasurface. Int J Mech Sci 2022; 214: 16. https://doi.org/10.1016/j.ijmecsci.2021.106928

[8]   Zhang J, Su X, Liu Y, Zhao Y, Jing Y, Hu N. Metasurface constituted by thin composite beams to steer flexural waves in thin plates. Int J Solids Struct 2019; 162: 14-20. https://doi.org/10.1016/j.ijsolstr.2018.11.025

[9]   Yuan S, Chen A, Wang Y. Switchable multifunctional fish-bone elastic metasurface for transmitted plate wave modulation. J Sound Vib 2020; 470: 13. https://doi.org/10.1016/j.jsv.2019.115168

[10]   Zhang S, Shu S, Bian X. Tunability for anomalous refraction of flexural wave in a magneto-elastic metasurface by magnetic field and pre-stress. Appl Phys Express 2022; 15(2): 6. https://doi.org/10.35848/1882-0786/ac4925

[11]   Wang Y, Wang Y, Wu B, Chen W, Wang Y. Tunable and Active Phononic Crystals and Metamaterials. Appl Mech Rev 2020; 72(4): 35. https://doi.org/10.1115/1.4046222

[12]   Zhang Q, Guo D, Hu G. Tailored Mechanical Metamaterials with Programmable Quasi-Zero-Stiffness Features for Full-Band Vibration Isolation. Advanced Functional Materials 2021; 31(33): 9. https://doi.org/10.1002/adfm.202101428

[13]   Casadei F, Ruzzene M, Dozio L, Cunefare K. Broadband vibration control through periodic arrays of resonant shunts: experimental investigation on plates. Smart Mater Struct 2010; 19(1): 13. https://doi.org/10.1088/0964-1726/19/1/015002

[14]   Airoldi L, Ruzzene M. Design of tunable acoustic metamaterials through periodic arrays of resonant shunted piezos. New J Phys 2011; 13: 21. https://doi.org/10.1088/1367-2630/13/11/113010

[15]   Fu Y, Shen C, Cao Y, Gao L, Chen H, Chan C, *et al*. Reversal of transmission and reflection based on acoustic metagratings with integer parity design. Nat Commun 2019; 10: 8. https://doi.org/10.1038/s41467-019-10377-9

[16]   Bing L, Huiyu X, Lingjuan H, Tianbao Y, Wenxing L, Tongbiao W, *et al*. Wide-angle asymmetric sound wave transmission in the single-layer metasurface. Technical Acoustics 2019; 38(3): 253-7.

[17]   Li B, Hu Y, Chen J, Su G, Liu Y, Zhao M, *et al*. Efficient Asymmetric Transmission of Elastic Waves in Thin Plates with Lossless Metasurfaces. Phys Rev Appl 2020; 14(5): 8. https://doi.org/10.1103/PhysRevApplied.14.054029

[18]   Yu N, Genevet P, Kats M, Aieta F, Tetienne J, Capasso F, *et al*. Light Propagation with Phase Discontinuities: Generalized Laws of Reflection and Refraction. Science 2011; 334(6054): 333-7. https://doi.org/10.1126/science.1210713

[19]   Shao S, Xia R, Li Z. Tunable piezoelectric metasurface for manipulating multi-mode guided waves in plate. Eng Struct 2022; 270: 12. https://doi.org/10.1016/j.engstruct.2022.114917

[20]   Wang W, Xu W, Yang Z, Yu X, Cheng S. Switchable bidirectional asymmetric transmission structure based on knob-controlled metasurfaces. Phys Lett A 2023; 490: 6. https://doi.org/10.1016/j.physleta.2023.129189

[21]   Zheng M, Park C, Liu X, Zhu R, Hu G, Kim Y. Non-resonant metasurface for broadband elastic wave mode splitting. Appl Phys Lett 2020; 116(17): 5. https://doi.org/10.1063/5.0005408

[22]   Zhang H, Chen Y, Liu X, Hu G. An asymmetric elastic metamaterial model for elastic wave cloaking. J Mech Phys Solids 2020; 135: 12. https://doi.org/10.1016/j.jmps.2019.103796

[23]   Pan R, Liu Z, Zhu W, Du S, Gu C, Li J. 3D Bended Metasurfaces: Asymmetrical Chirality in 3D Bended Metasurface (Adv. Funct. Mater. 31/2021). Advanced Functional Materials 2021; 31(31).

[24]   Fan H, Luo J. Research progress of non-Hermitian electromagnetic metasurfaces. Acta Phys Sin 2022; 71(24): 16. https://doi.org/10.7498/aps.71.20221706

[25]   Chung C, Lai F, Huang S, Chen Y. Anisotropic Metasurface With Asymmetric Propagation of Electromagnetic Waves and Enhancements of Antenna Gain. IEEE Access 2021; 9: 90295-305. https://doi.org/10.1109/access.2021.3091464

[26]   Wang X, Fang X, Mao D, Jing Y, Li Y. Extremely Asymmetrical Acoustic Metasurface Mirror at the Exceptional Point. Phys Rev Lett 2019; 123(21): 6. https://doi.org/10.1103/PhysRevLett.123.214302

[27]   Zhang X, Li L, Li K, Liu T, Zhang J, Hu N. Flexural wave splitting via elastic metagratings based on high-order diffraction theory. Appl Acoust 2023; 202: 11. https://doi.org/10.1016/j.apacoust.2022.109170

[28]   Li H, Hu Y, Huang H, Chen J, Zhao M, Li B. Broadband low-frequency vibration attenuation in 3D printed composite meta-lattice sandwich structures. Compos Pt B-Eng 2021; 215: 15. https://doi.org/10.1016/j.compositesb.2021.108772

[29]   Li C, Song Z. Tailoring terahertz wavefront with state switching in VO2 Pancharatnam-Berry metasurfaces. Opt Laser Technol 2023; 157: 9. https://doi.org/10.1016/j.optlastec.2022.108764

[30]   Fan Y, Wang J, Fu X, Li Y, Pang Y, Zheng L, *et al*. Recent developments of metamaterials/metasurfaces for RCS reduction. EPJ Applied Metamaterials 2019; 6: 15.

[31]   Shen Y, Xu Y, Liu F, Yang Z. Metasurface-guided flexural waves and their manipulations. Int J Mech Sci 2023; 257: 15. https://doi.org/10.1016/j.ijmecsci.2023.108538